Original scientific paper

Effect of KOH concentration on corrosion behavior and surface morphology of stainless steel 316L for HHO generator application

Basori Basori[1,2], Wan M. F. W. Mohamad[2,3,✉], Muhd R. Mansor[2,3], Noreffendy Tamaldin[2,3], Agung Iswadi[1], Maman K. Ajiriyanto[4] and Ferry Budhi Susetyo[5]

[1]Department of Mechanical Engineering, Faculty of Engineering and Science, Universitas Nasional, Sawo Manila, Pasar Minggu, Jakarta 12520, Indonesia
[2]Fakulti Kejuruteraan Mekanikal, Universiti Teknikal Malaysia Melaka, Hang Tuah Jaya, 76100 Durian Tunggal, Melaka, Malaysia
[3]Centre for Advanced Research on Energy, Universiti Teknikal Malaysia Melaka, Hang Tuah Jaya, 76100 Durian Tunggal, Melaka, Malaysia
[4]Research Center for Nuclear Fuel Cycle and Radioactive Waste Technology – National Research and Innovation Agency (BRIN), 15314, Indonesia
[5]Department of Mechanical Engineering, Universitas Negeri Jakarta, Jakarta 13220, Indonesia
Corresponding author: ✉farid@utem.edu.my

Abstract

Hydrogen production could be enhanced by increasing the potassium hydroxide (KOH) concentration, but higher KOH concentrations result in higher corrosion rates. Therefore, a deep investigation of the electrochemical behavior of stainless steel (SS 316L) in the KOH solution is needed. This study investigates the influence of KOH concentrations on the electrochemical behavior, surface morphology, structure, and sample phases of SS 316L. The investigations were conducted by some electrochemical techniques, UV-vis, scanning electron microscopy-energy dispersive spectroscopy (SEM-EDS), and X-ray diffraction (XRD). The corrosion rate was found to increase, and solution resistance to decrease with increasing KOH concentration. Samples tested in 5, 30, and 50 g l^{-1} of KOH showed corrosion rates of 0.457, 2.362, and 5.613 µm year^{-1}, respectively. A wide passive region and the noblest pitting potential were noticed for the sample with 5 g l^{-1} of KOH. Moreover, Mott-Schottky plots and characteristic wavelengths of UV-Vis suggest the formation of iron and chromium oxides by the passivation of samples. The SEM analysis showed a dynamic change of surface morphology from the lowest to the highest concentration with the intergranular corrosion found at the grain boundaries area. In conclusion, concentrations < 50 g l^{-1} KOH could be recommended since they would support the optimum remaining life of SS 316 L plates in HHO generators.

Keywords
Corrosion rate; KOH media; passive film; hydrogen generator

Introduction

Fossil fuels are about 82 % of the world's energy demand for a combustion engines. Fossil fuels generate the main greenhouse gas problem contributing to global warming and climate change [1]. With the increase in energy demand, innovations must be developed and produced to supply clean and affordable energy.

Hydrogen is a promising renewable source of clean energy and environmentally friendly [2-4]. Hydrogen indeed could play an essential role as one of the possible solutions towards climate change adaptation and decarbonization agenda. Many studies have been done for years to develop an optimum system for hydrogen production. One study in Turkey analyzed the cost of hydrogen production *via* an electrolysis system supplied by wind energy [5]. Another study emphasized that hydrogen produced from renewable energy could help to overcome the intermittency of renewable sources, which could be a problem in isolated territories. Thus, a life cycle assessment covering hydrogen production and consumption in an isolated area was performed [6]. Another study also provided an analysis of the life cycle assessment for hydrogen production using the electrolysis system by considering the improvement of material demand, system efficiency, and cell lifetime [7]. This study indicated that the high material demand with high system efficiency (HDHE) reduces carbon emission by up to 15.5 % compared to the current state of the electrolysis system.

Hydrogen could be produced through a water electrolysis system. Apart from the electrolysis system types, several previous studies were focused on increasing oxy-hydrogen (HHO) gas production, rather than the performance of the material used for the generator system itself [8-12]. HHO gas production can be optimized by determining electrolyte concentration, operating temperature, and large cell gap. Choodum *et al.* [9] reported that using a closed-loop HHO production system, the number of cells and applied current were the two main parameters affecting the HHO gas production rate. Based on the numerical simulation, it was discovered that by using 200 cells with 40 A of current at 80 °C, 64 l min^{-1} of hydrogen gas could be produced [9]. Subramanian and Thangavel [10] also reported that increased electrolyte concentration from 0.25 M to 1.0 M of sodium hydroxide (NaOH) enhances conductivity and decreases electrical potential. Similar to that report, the influence of variation in electrolyte concentration and applied current was also studied to find the optimum configuration of the water electrolysis system for HHO gas production [12]. It was found that a combination of 0.05 M NaOH concentration with applied current of 15 A produced the highest volume of HHO gas up to 0.925 l min^{-1} with 89.13 % of electric current efficiency [12].

Besides NaOH, potassium hydroxide (KOH) is preferred for hydrogen production because it has higher conductivity than NaOH due to the ionic conductivity of K$^+$ being higher than Na$^+$ [13-15]. Moreover, the overall production efficiency of hydrogen in 3 M KOH and 3 M NaOH at standard conditions resulted in an efficiency of 90.25 and 83.33 %, respectively [14]. Hydrogen production through KOH increased with an increase in the KOH concentration. An increase from 1 to 2 mol of KOH could increase gas production from 55 to 75 cm^3 min^{-1} at 10 V and 2 A [16]. Moreover, Purwondho *et al.* [17] conducted hydrogen gas production by 5, 10, 15, 20, and 25 g l^{-1} of KOH, resulting in approximately 14, 26, 27, 31, and 62 ml min^{-1}, respectively. Increasing the KOH concentration could also increase the corrosion rate of electrodes [18]. As discussed by Subramanian and Ismail [19], the cost associated with the periodic replacement of electrodes due to corrosion is one of the crucial challenges to be mitigated in the water electrolysis system for the HHO generator. Various electrodes, such as stainless steel, SS 316L, SS 304, and copper (Cu) alloys, are commonly used for hydrogen production. A comparison of the corrosion behavior of these materials in water electrolysis using KOH solution was carried out, and SS 316 L exhibited the highest corrosion

resistance among three metals tested [20]. Olivares-Ramírez *et al.* [21] studied different stainless steel in KOH and NaOH solutions. They found that SS 316 L is the perfect electrode material in KOH, due to producing a similar volume of hydrogen gas for less time. This phenomenon is due to the higher nickel content and stabilized oxide resistivity [22,23]. Furthermore, SS 316 L has density of 7.99 g cm^{-3} and equivalent weight of 27.56 g mol^{-1} [24].

This study investigates the effect of KOH solution on the electrochemical behavior of SS 316 L, surface morphology, phases, and structure. Varying concentrations of KOH solution are used to compare factors in identifying the most favorable KOH concentration for SS 316 L. The use of KOH solution with various concentrations was also recommended by Purwondho *et al.* [17], who observed higher gas production by increasing KOH concentration. Investigating SS 316 L in KOH solution with varying concentrations is expected to discover a new promising option for metal plates and electrolyte solution for utilization in the HHO system generator. Thus, the investigation of SS 316 L performance against corrosion carried out in this study would contribute to a better understanding and improve the feasibility of the electrolysis system for the HHO generator.

Experimental

Materials

The SS 316 L plate with a thickness of 0.3 mm was used as an experimental specimen. SS 316 L was chosen as a substrate due to its superior corrosion resistance compared to alloy 304/304 L. Its excellent properties make it a suitable candidate for an electrode plate applied to HHO generator systems. The chemical composition of the SS 316 L is shown in Table 1. Samples were subjected to the open circuit potential measurements, potentiodynamic polarization, electrochemical impedance spectroscopy, and Mott-Schottky test in KOH solutions (Sigma Aldrich) of different concentrations. Electrochemical measurements are referred to treated samples, and the untreated (blank) sample is used for the comparison.

SS 316 L samples in concentrations of electrolyte of 5, 30, and 50 g l^{-1} KOH, were denoted as K5, K30, and K50, respectively. The concentration of the electrolyte solution affects the production of HHO gas. A few studies revealed that the production of hydrogen gas increased with the increasing alkaline concentration of KOH solution [25-27], and consequently, the electrode plates used in high concentrations may be degraded due to corrosion. Therefore, in this study, electrochemical cor-rosion tests were carried out at intervals of 5 to 50 g l^{-1} to determine the level of corrosion resistance of SS 316 L plates.

Table 1. *Chemical composition of SS 316 L*

Element	Cr	Ni	Mn	Mo	C	Fe
Content, wt.%	16.33	9.97	2.06	1.95	<0.1	balance

Electrochemical measurements

The SS 316 L plates were cut and then mounted in a holder with an exposure area of 1 cm². The samples were polished with grit 1000 up to 2000 and cleaned with acetone before open circuit potential (OCP) measurement was conducted. To reach steady voltage, OCP measurement was performed during 7200 s in 5, 10, and 50 g l^{-1} of KOH, respectively.

A potentiodynamic polarization method was carried out to determine the corrosion resistance of the SS 316 L. The potentiodynamic polarization was conducted in KOH solutions with varying concen-trations (5, 30, and 50 g l^{-1}). The potentiodynamic polarization test used the Gamry Reference 600

potentiostat. The saturated calomel electrode (SCE) was used for the reference electrode (RE), and platinum wire was used for the counter electrode (CE). The potentiodynamic polarization measurements were performed from -0.250 to +1.500 V with a scan rate of 2 mV s^{-1}. It was already reported that a slower scan rate (0.1 mV s^{-1}) could lead to a significant change in the interfacial structure [28] and a more corroded surface [29]. On the other hand, the higher scan rate could cause a disturbance of the charging current and lead to misinterpretation of data [28,29]. Therefore, 2 mV s^{-1} was expected to be the appropriate scan rate at the potential range used in this study (-0.250 to +1.500 V).

The corrosion rate of samples was calculated by the following expression [30]:

$$CR = \frac{CMj_{corr}}{n\rho} \tag{1}$$

where CR / mm year^{-1} is corrosion rate, C = 3.27 is constant, M / g mol^{-1} is atomic weight, j_{corr} / A cm^{-2} is corrosion current density, ρ / g cm^{-3} is the density of material sample and n is the number of electrons involved.

The electrochemical impedance spectroscopy (EIS) measurements were also carried out by applying Gamry potentiostat Reference 600 equipped for EIS measurements. EIS was measured at OCP, in the frequency range of 100 000 - 0.2 Hz and alternating signal of 10 mV amplitude. The Mott-Schottky plots were determined by EIS equipment at the frequency of 1000 Hz and potential changes from -2 to +2 V. All electrochemical measurements were performed at 30 °C.

For UV-Vis spectroscopy, Shimadzu UVMINI 1240 was used for measurement at wavelengths 207-250 nm.

Surface morphology observation

Surface morphology was observed using scanning electron microscopy with energy dispersive spectroscopy (SEM-EDS). Thermo-scientific SEM-EDS of the Phenom Pharos type was used with a magnification of 2500×. These observations were conducted after potentiodynamic polarization experiments were performed in 5, 30, and 50 g l^{-1} of KOH, respectively.

X-ray diffraction (XRD) analysis

XRD (PANalytical with Co K radiation) was conducted with a step size of 0.02° from 30° until 70°. XRD was conducted for an untreated (blank) sample and treated samples after potentiodynamic polarization experiments were performed in 5 and 50 g l^{-1} of KOH, respectively. A high score plus software was used to find sample patterns.

Results and discussion

Open circuit potential (OCP)

The measurement of OCP as a function of time is shown in Figure 1. OCP of K5 sample slowly increases, while OCPs of K30 and K50 increase sharply to get a steady state. Overall, all curves show the same tendency to increase OCP to a more positive value. It is well known that a rise of OCP to positive values indicates the formation of passive and protective film, while its moving to a negative direction would indicate broken film, unformed film, or dissolution of the film [31]. OCP of K50 reached a steady state at 4500 s, while other samples needed time over 7200 s. This means that for K50 sample, a protective passive film on the SS 316 has been formed in 4500 s [32]. This behavior indicates that decreasing KOH concentration shifts OCP to a more positive value. Wojciechowski *et al*. [33] found similar behavior when OCP of SS 316 L was performed in 1 and 6 M KOH. It can also be noticed in Figure 1 that the initial OCP value of the K30 and K50 samples is more negative than

K5, indicating that the K5 sample possessed a thicker native oxide film than others [34]. Moreover, at all immersion times, K5 showed more noble OCP than others [33], which suggests that a more protective passive layer is formed on the surface SS 316 L showing less corrosion rate [31]. The passive film could slow down the dissolution of steel due to the stability of the passive film [35,36]. This result fully agrees with corrosion rates obtained by the potentiodynamic polarization tests described in the following section.
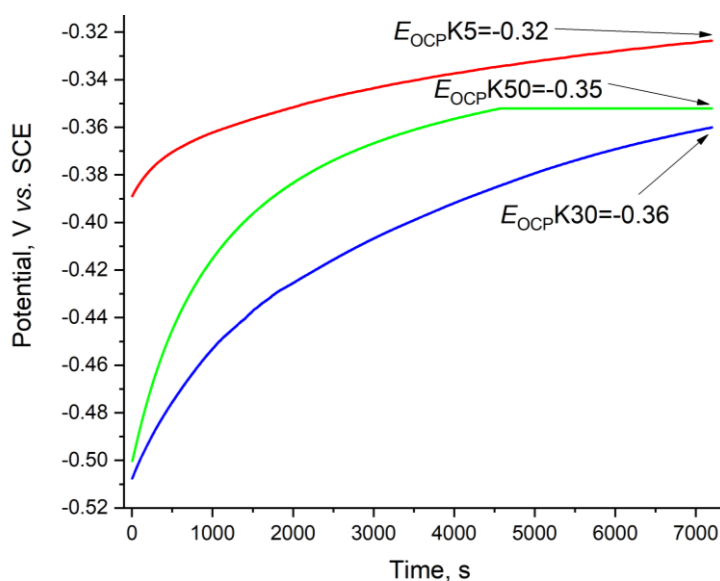
Figure 1. *Open circuit potential curves of SS 316 L in various KOH solutions*

Potentiodynamic polarization

Potentiodynamic polarization was performed to find out the electrochemical behavior of the samples. Figure 2 represents the electrochemical polarization of SS 316 L in various concentrations of KOH. Three different potential regions are shown in the potentiodynamic polarization curves, which include: (i) active region, (ii) passive region, and (iii) transpassive region [37,38]. It seems that the K5 sample has a wider passive region than other samples. Based on the OCP, K5 is nobler and could have a more protective passive layer. Protective passive film is related to the surface complex oxide, which is confirmed by EDS and Mott-Schottky results. Oxide on the SS 316 L is associated with Cr_2O_3, NiO, and Fe_2O_3 [37,39]. The K5 sample has less corrosion rate than other samples because it has a wider passive region. As we know, passivation is one of the most influential factors in the corrosion resistance of the sample [40].

Based on Figure 2, an increase in the electrolyte concentration leads to a decrease in the passive area region. Krawczyk *et al.* found that passive behavior is associated with the sudden drop of current density with the potential, occurring as a function of the electrolyte concentration [41]. Commonly before passivation, a metal dissolution, *i.e.,* uniform corrosion process, occurs in the active loop on the SS 316 L. A primary surface film formed during the active loop consists of Cr_2O_3 [41]. Sample K30 and K50 have an active loop that is not prominent for the K5 sample.

K5 sample produces a pitting potential (E_{pit}) at the highest value of around 0.8 V. E_{pit} is the lowest potential where the passive film is still stable prior to breakdown potential where aggressive species in the electrolyte solution could penetrate the films [34]. The breaking down of the film is indicated by the significant current increase. Thus, the higher the E_{pit} value, the sample is more resistant to corrosion [41]. This behavior may be due to the surface with more oxygen based on the EDS observation shown below.
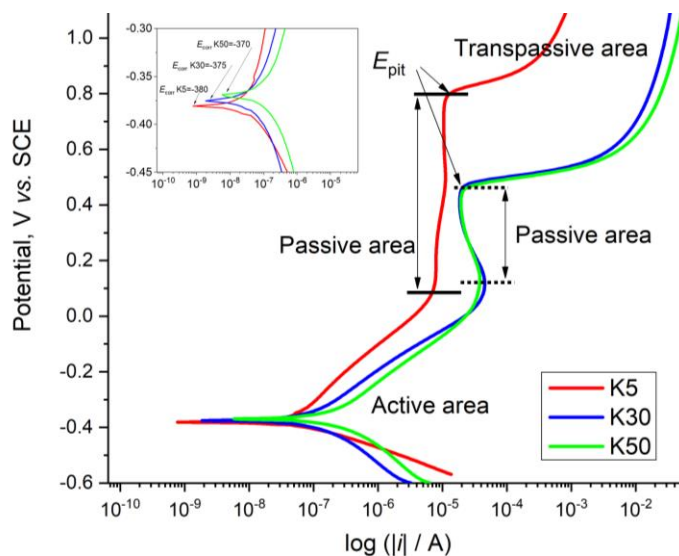
***Figure 2.** Potentiodynamic polarization curves of SS316L samples*

The polarization curves in Figure 2 show that the concentration of KOH affects the corrosion rate. The higher the concentration of KOH, the higher the corrosion current or corrosion rate. Hamidah *et al.* [18] also reported that the higher the concentration of KOH, the higher the corrosion rate of SS 316. The higher concentration of KOH produces a polarization curve that shifts further to the right, indicating an increase in corrosion current, as shown in Figure 2. This argument can be corroborated by the corrosion rate data in Table 2, showing the highest corrosion rate of 5.613 μm year^{-1} for the K50 sample. In comparison, the K5 produced the lowest corrosion rate of 0.457 μm year^{-1}. This finding is aligned with a previous study that found a higher corrosion rate of SS 316 L at higher concentrations of electrolyte solution [37].

***Table 2.** Parameters determined from potentiodynamic polarization curves and corrosion rates calculated by eq. (1)*

Sample	E_{corr} / V *vs.* SCE	I_{corr} / nA	Corrosion rate, μm year^{-1}
K5	-0.380	19.65	0.457
K30	-0.375	103.20	2.362
K50	-0.370	245.50	5.613

The HHO gas formation rate from 1 to 2 mol concentration increases linearly [16]. Moreover, other research was conducted on HHO gas production using 5, 10, 15, 20, and 25 g l^{-1} of KOH, resulting in approximately 14, 26, 27, 31, and 62 ml min^{-1} [17]. An increase in the production of HHO gas is needed, but it is necessary to pay attention to the impact on the damage or corrosion experienced by the electrode (SS316L plate). Therefore, corrosion analysis is needed to determine the optimum concentration in the electrolysis of the HHO gas production process. Corrosion analysis using Tafel extrapolation for a concentration of 5 - 50 g l^{-1} can explain that a concentration range of 5 - 50 g l^{-1} produces a fairly low corrosion rate < 7.620 μm year^{-1}. Performing a higher concentration than 50 g l^{-1} might have a worse impact, such as pitting corrosion, that could affect the whole HHO system.

Electrochemical impedance spectroscopy (EIS)

Figure 3 presents Nyquist impedance plots of SS 316 L samples measured at OCP in various concentrations of KOH. The imaginary impedance against the real component showed a single capacitive

arc for all specimens. The capacitive arc is highest for K5 and lowest for the K50 sample, but the differences are small. Generally, a high capacitive arc corresponds to low metal dissolution since the diameter of the arc is related to the charge transfer resistance at SS 316 L-KOH solution interface [42].
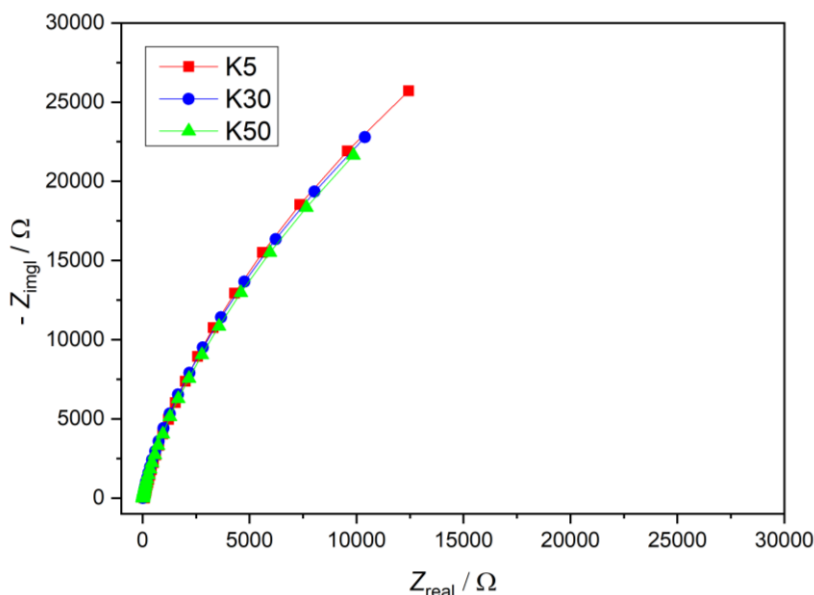
Figure 3. *Nyquist plots of SS316L samples*

The experimental results of EIS in the form of Bode diagrams are presented in Figure 4. The total impedance behavior presented as the log of impedance magnitude and phase angle against the log of applied frequency is shown in the Bode plot. At high frequencies, the solution resistance (R_s) could be assessed from log |Z| horizontal line (zero phase angle). As expected, R_s is dependent on the concentration of KOH and is the highest for K5 (less conductive) and lowest for K50 (more conductive) sample. Capacitive charging of the solid-liquid interface occurs at medium to lower frequencies and is seen as about -1 sloping line in the log |Z| plot, coupled with a phase angle tending to -90°. Native (oxide) passive film properties of the surface layer could be provided by this capacitive impedance. A prominent and near equal capacitive impedance response for all samples suggests low corrosive systems, *i.e.,* systems with very high charge transfer (R_{ct}) values. In impedance plots, R_{ct} contributes to the overall impedance at low frequencies. In Figure 4, due to very high R_{ct} values for all samples, their contribution is best seen from the decrease of phase angles within a decade of the lowest frequencies. The value of R_{ct} could be, together with other impedance parameters, determined by impedance curve fitting procedure and corresponding electric equivalent circuit (EEC) [43].

Resistance (R_s and R_{ct}) values of SS 316 L are presented in Table 3. The determination of R_s and R_{ct} values was performed by fitting the EEC drawn in Figure 4 to experimentally measured impedance spectra. The solution resistance (R_s) and charge transfer resistance (R_{ct}) values decrease with the increase in KOH concentration. The decrease in the charge transfer resistance of the samples suggests a rise in the corrosion rate. This is supported by potentiodynamic polarization results, where the corrosion rate increases with increased KOH concentration.

Table 3. *EIS resistance results*

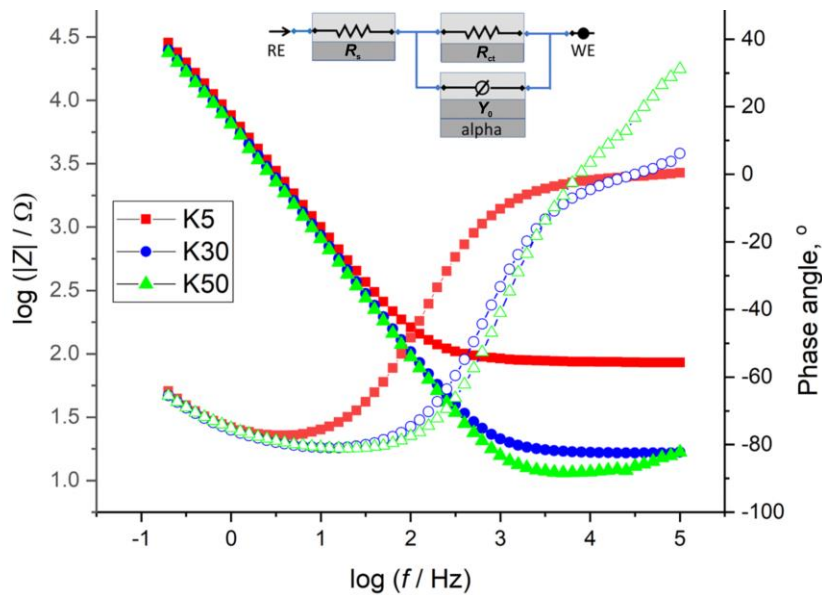| Sample	R_s / Ω	R_{ct} / kΩ
K5	86.51	95
K30	16.36	73
K50	11.63	61

Figure 4. Bode plots of SS 316 L samples

Mott-Schottky analysis

Figure 5 presents the Mott-Schottky curves of SS 316 L in various concentrations of KOH. Measurements in both positive and negative potential directions were conducted. However, there is a difference in semiconductor properties between K5 and K30 or K50 samples. Sample K5 has a turning potential of -0.75, -0.5 and 0.5 V *vs.* SCE. Both samples K30 and K50 have a turning potential of 0.5 V *vs.* SCE if any. The negative slope in the second region is attributed to p-type, and the positive slope in the first and third regions is indicated as n-type [44]. In previous studies, curves were measured in the positive direction [45,46]. Therefore, in the present work, the positive direction was used to explain the semiconducting properties of the SS 316 L in various concentrations of KOH.
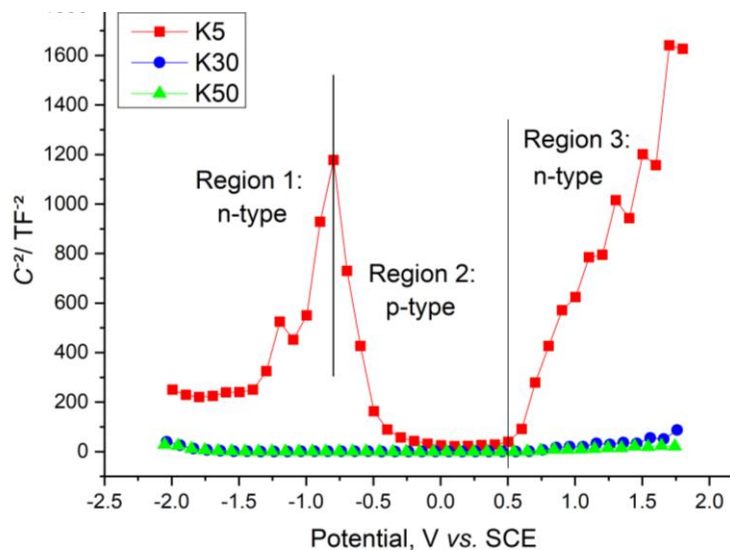

Figure 5. Mott-Schottky plots of SS 316 L samples

The curve increases linearly when the potentials are between +0.50 and +1.75 V *vs.* SCE. This behavior is due to the space layer of the oxide film of SS 316 L (passive film) formed with the applied potential according to the following n-type and p-type equations (2) and (3) [39,47]:

$$\frac{1}{C^2} = \frac{2}{\varepsilon\varepsilon_0 e N_d A^2}\left(E - E_{fb} - \frac{KT}{e}\right) \text{ n-type} \tag{2}$$

$$\frac{1}{C^2} = \frac{2}{\varepsilon \varepsilon_0 e N_a A^2}\left(E - E_{fb} - \frac{KT}{e}\right) \text{ p-type} \tag{3}$$

where ε_0 = 885.4 pF cm^{-1} is permittivity of free space, ε = 12 is relative dielectric constant, e = 1.6×10^{-19} C is charge of the electron, N_d / cm^{-3} is donor density, N_a / cm^{-3} is acceptor density, A / cm^2 is surface area of the sample, E / V is applied potential, E_{fb} / V is flat band potential, k = 1.38×10^{-23} J K^{-1} is Boltzmann constant,; and T / K is absolute temperature.

Potentials around 0 to +0.5 and +0.5 to +1.75 V *vs*. SCE represent p-type and n-type, respectively. At the flat band potential (p-type), Cr_2O_3 is forming. For lower potential (n-type), NiO and Cr_2O_3 are created, and then for higher potential (n-type), Fe_2O_3 forms [39,48,49]. This means that between 0 and +1.75 V, Cr_2O_3 and Fe_2O_3 are probably formed, which can be supported by EDS results presented below, which show the presence of chromium, iron, and oxygen on the surface of treated SS 316.

UV- Vis measurements

UV-Vis of KOH solutions has been conducted, and the results are presented in Figure 6. Uv-Vis was recorded in various concentrations of KOH after potentiodynamic polarization measurement to prove the possible presence of particles in the solution [50].
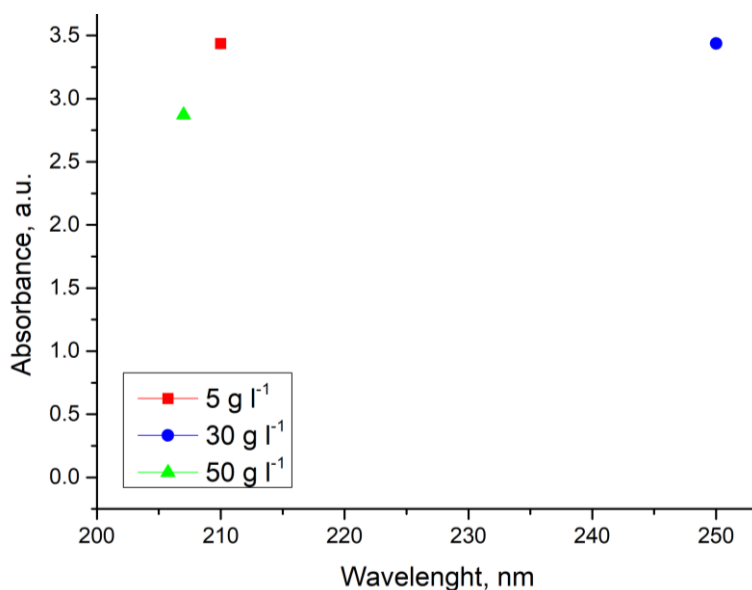

Figure 6. *UV-Vis measurements of KOH solutions*

Samples of concentrations of 5, 30, and 50 g l^{-1} KOH showed wavelength peaks at 210, 250, and 210 nm after being used for potentiodynamic polarization measurement. Maximum absorbance and wavelength are different for various samples because the Uv-vis plot shape is sensitive to particle size [51] and their concentration. El Kemari *et al.* have found that increased NiO concentration increases absorbance at similar wavelengths [52]. Based on the UV-Vis, some particles are shown in the solution after potentiodynamic polarization. It is known that Cr_2O_3, NiO, and iron oxide wavelength intensities are around 250, 330, and 200-220 nm, respectively [52–54]. Therefore, those particles as oxides are obviously present in the KOH solution after potentiodynamic polarization tests.

Surface morphology observation using SEM-EDS

Figure 7 shows the surface morphology of treated SS 316 L. SEM-EDS tests were carried out to examine the influence of increasing KOH concentration on the surface morphology and composition

of the samples. It is found that the surface changed gradually, exhibiting white rust forms on sample surfaces. As defined by Nasrazadani *et al*. [55], white rust (oxide) occurs in the grain boundaries area. Du *et al*. [56] found that white rust accumulating at the grain boundaries may refer to intergranular corrosion. White rust is associated with oxide and in Figure 7, it can be especially seen at grain boundaries of K5 and K50 samples. According to the Mott-Schottky measurement, different oxides could be specified by p-type on n-type properties. In the voltage range voltage between -2 and +2 V, sample K5 clearly showed n-type and p-type properties. In addition, the surface of the K30 sample was found to be more homogeneous than the K50 sample. A similar finding was reported by Galindo-Luna *et al.* [57], who found that NaOH-H_2O solution with a concentration of 50 wt.% caused detached flakes on the steel surface. In comparison, a more homogeneous and compact surface was found on the sample using a concentration of 40 wt.% [57].
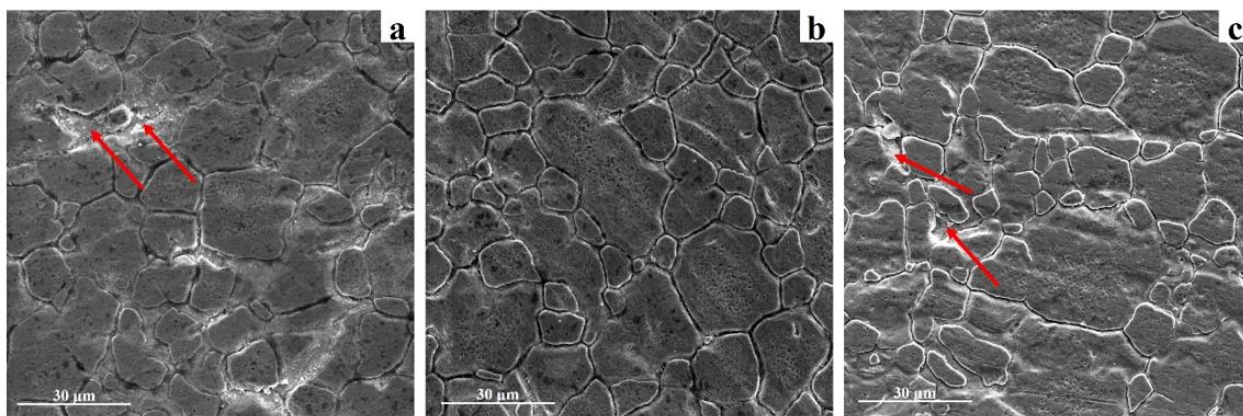
Figure 7. *SEM micrographs of SS 316L samples: (a) K5, (b) K30, and (c) K50*

The EDS analysis was carried out to identify the phases on the SS 316L sample surfaces at the grain boundaries area, as shown in Figure 8. The results for all samples are in general agreement with the composition of SS 316L given in Table 1, showing the presence of Fe, Cr, Ni, and Mo as main surface elements and oxygen as the additional element. The content of the oxygen element for the K5 sample was higher than other samples, which refers to a better passivation process on the K5 sample. For the K5 sample, some other additional elements (Al, Si, K, Ca) appeared on the surface. Interestingly, the potassium (K) element could not be found on the surfaces of the K30 and K50 samples. Hamidah *et al.* [18,20] found that the percentage of K element deposited on the surface of the sample tested for corrosion in 0.27 M KOH was about 2.15 wt.%, comparable with 1.9 wt.% found in this study.

EDS chemical composition testing carried out in this study was based on the spot mode by selecting only a few specific locations. This means that the chemical composition results might not fully represent the whole sample surface. Also, the washing process performed after corrosion tests could cause the elimination of the K element for K30 and K50 samples, where K was not identified by EDS. The identified element K at the K5 sample is considered an impurity based on the solution settled and trapped on the surface of the corroded sample or at the grain boundaries. The grain boundaries of the SS 316 L sample are the parts that have high energy compared to the grain or matrix areas. Consequently, they are more easily corroded and allow the presence of elemental deposits from electrolytes in the grain boundary area. However, it is worth noting that based on the SEM micrographs and EDS analysis, the K30 sample exhibited better surface morphology than the K50 sample.
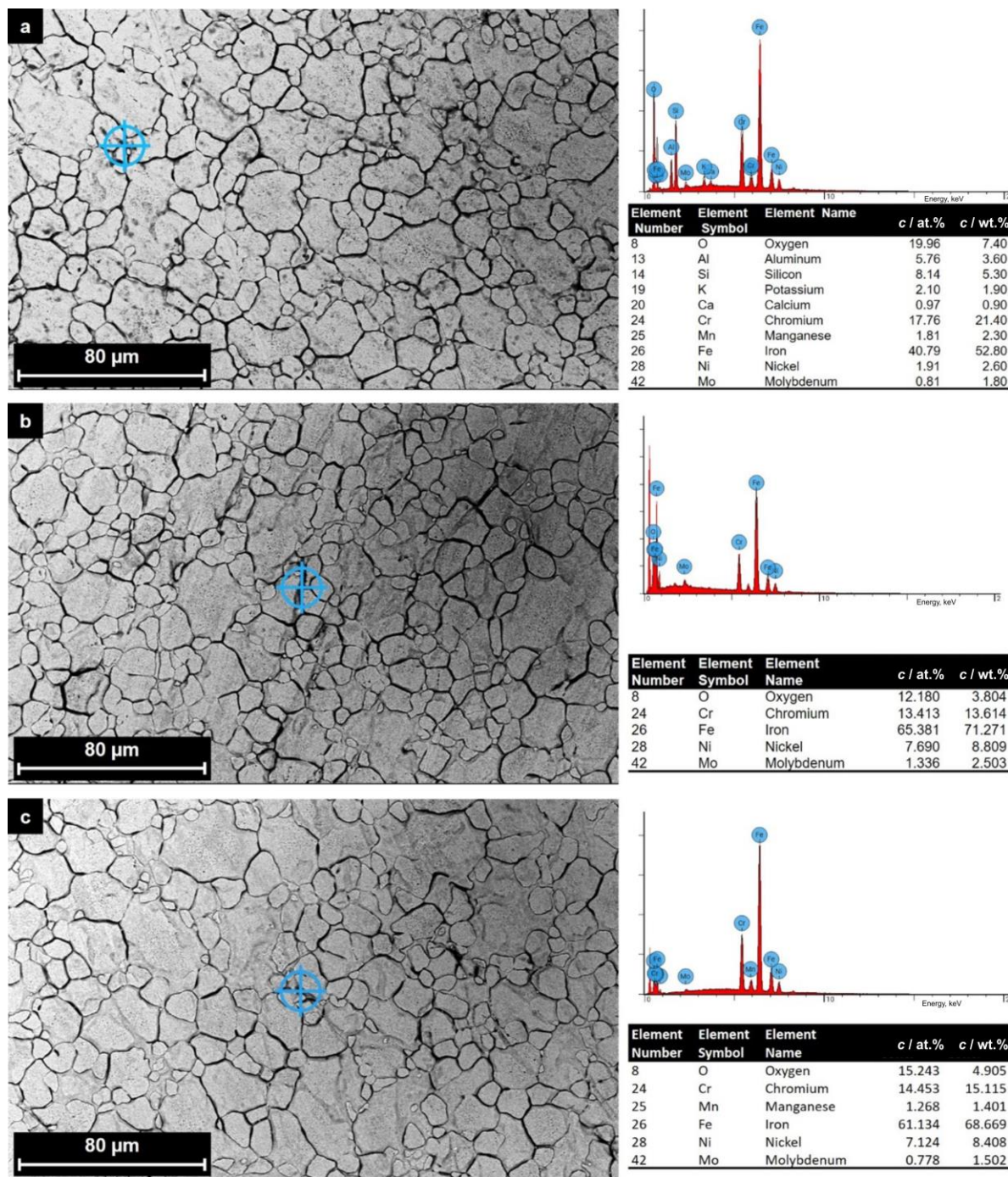
Figure 8. *EDS analysis of SS316L samples: (a) K5, (b) K30, and (c) K50*

Structure analysis of corroded surfaces using XRD

The electrochemically treated and untreated samples were analyzed by XRD, as shown in Figure 9. The XRD curves showed peaks around 51° and 59.7° identified as austenite (γ-Fe). The diffraction patterns for all samples are the same, suggesting the presence of only the γ-Fe phase. The corrosion process in the KOH solution did not produce a new phase or compound, although the SEM-EDS results showed the presence of oxygen elements on the surface. Because the oxygen content was relatively low, the corrosion product in the form of a new compound or phase was not identified. Treated samples, however, showed decreased peak heights compared to the untreated sample. Chai *et al.* [58] found that surface modification causes more roughness that can lead to a decrease of peak heights. It seems that in the present experiments, treated K5 and K50 samples changed their

surface roughness by corrosion during potentiodynamic polarization tests, which resulted in a decrease of XRD peaks at around 51° and 58°.
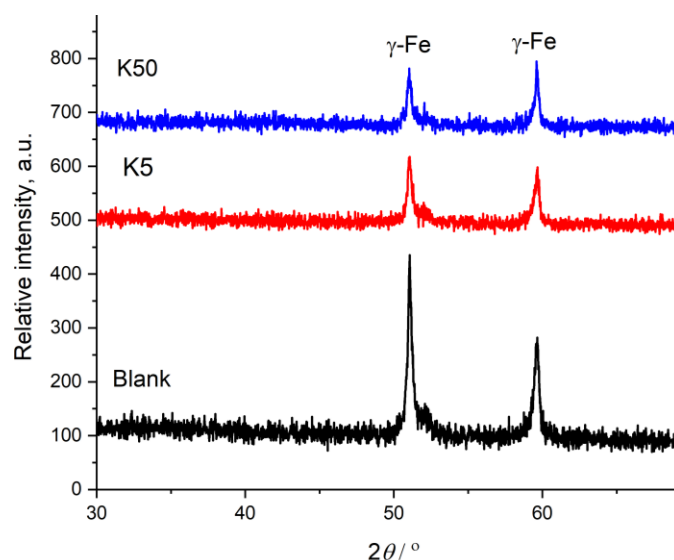
Figure 9. *XRD patterns of untreated and treated SS 316 L samples*

Conclusions

The influence of the concentration of KOH on the morphology, structure, phase, and corrosion behavior of SS 316L was studied using surface and electrochemical methods. The conclusions of the research are presented as follows.

1. The corrosion rate of the SS 316L plate increased along with an increase of KOH concentration from 5 to 50 g l^{-1}.

2. A wider passive region and more noble pitting potential was found for the SS316L in the lowest concentration of KOH solution (5 g l^{-1}) compared to higher concentrations (30 and 50 g l^{-1}).

3. The solution resistance (R_s) and charge transfer resistance (R_{ct}) determined by EIS were decreased with the growth of KOH concentration. These results suggested a rise in solution conductivity and corrosion rate of SS 316L with an increase in KOH concentration.

4. At potentials between 0 and 1.75 V *vs.* SCE, Mott-Schottky plots suggested the formation of Cr_2O_3 and Fe_2O_3 passive films on sample surfaces. M-S response was found much more prominent for a lower concentration of KOH (5 g l^{-1}), suggesting the formation of a well-defined semiconductive passive film in this case.

5. As seen by UV-vis, some particles are present in the KOH solution after the potentiodynamic polarization test. On the basis of characteristic wavelengths, these particles could be identified as Fe, Ni and Cr oxides.

6. The intergranular corrosion phenomenon was prominent at the grain boundaries area, as seen by white rust in SEM images. At these places, EDS analysis suggested the presence of oxygen in addition to Fe, Ni and Cr as main components. The content of oxygen was higher for the solution containing 5 g l^{-1} KOH than for other solutions.

7. The corrosion process in the KOH solution, however, did not produce a new phase or compound on the SS 316L surface. Only the austenite phase was detected for all concentrations of KOH solution, while decreased XRD peak heights of treated samples indicate an increase in surface roughness of SS 316L.

8. On the basis of obtained results, utilization of < 50 g l^{-1} of KOH concentration could be recommended for the HHO generator with SS 316L plates. Low corrosion rates in these cases

would support the optimum useful life of the SS 316L plate electrodes in the HHO generator system.

References

[1]   M. A. El Kady, A. El Fatih Farrag, M. S. Gad, A. K. El Soly, H. M. Abu Hashish, Parametric study and experimental investigation of hydroxy (HHO) production using dry cell, *Fuel* **282** (2020) 118825. https://doi.org/10.1016/j.fuel.2020.118825

[2]   T. Nabil, M. M. K. Dawood, Enabling efficient use of oxy-hydrogen gas (HHO) in selected engineering applications; transportation and sustainable power generation, *Journal of Cleaner Production* **237** (2019) 117798. https://doi.org/10.1016/j.jclepro.2019.117798

[3]   M. M. A. Sayed, M. S. Shalaby, W. Rady, W. Hussien, M. Magdy, K. El-Sabagh, A. Mohamed, A. Nour Eldin, F. Maher, M. Osama, Design of HHO cell as energy source for electric vehicles, *IOP Conference Series: Materials Science and Engineering* **610** (2019) 012089. https://doi.org/10.1088/1757-899X/610/1/012089

[4]   H. Adamu, M. Qamar, Routes to enhanced performance of electrolytic hydrogen evolution reaction over the carbon-encapsulated transition metal alloys, *Journal of Electrochemical Science and Engineering* **12** (2022) 947–974. https://doi.org/10.5599/jese.1446

[5]   M. S. Genç, M. Çelik, I. Karasu, A review on wind energy and wind-hydrogen production in Turkey: A case study of hydrogen production *via* electrolysis system supplied by wind energy conversion system in Central Anatolian Turkey, *Renewable and Sustainable Energy Reviews* **16** (2012) 6631–6646. https://doi.org/10.1016/j.rser.2012.08.011

[6]   G. Zhao, A. S. Pedersen, Life Cycle Assessment of Hydrogen Production and Consumption in an Isolated Territory, *Procedia CIRP* **69** (2018) 529–533. https://doi.org/10.1016/j.procir.2017.11.100

[7]   E. Schropp, G. Naumann, M. Gaderer, Prospective Life Cycle Assessment: A Case Study of Hydrogen Production with Water Electrolysis, *Procedia CIRP* **105** (2022) 92–97. https://doi.org/10.1016/j.procir.2022.02.016

[8]   A. Sudrajat, E. Mayfa Handayani, N. Tamaldin, A. Kamal Mat Yamin, Principle of generator HHO hybrid multistack type production technologies to increase HHO gas volume, *SHS Web of Conferences* **49** (2018) 02016. https://doi.org/10.1051/shsconf/20184902016

[9]   N. Choodum, C. Sangwichien, R. Yamsaengsung, Optimization of a closed-loop HHO production system for vehicles and houses, *Environmental Progress and Sustainable Energy* **38** (2019) 268–277. https://doi.org/10.1002/ep.12909

[10]   B. Subramanian, V. Thangavel, Analysis of onsite HHO gas generation system, *International Journal of Hydrogen Energy* **45** (2020) 14218–14231. https://doi.org/10.1016/j.ijhydene.2020.03.159

[11]   H. Tebibel, A. Khellaf, S. Menia, I. Nouicer, Design, modelling and optimal power and hydrogen management strategy of an off grid PV system for hydrogen production using methanol electrolysis, *International Journal of Hydrogen Energy* **42** (2017) 14950–14967. https://doi.org/10.1016/j.ijhydene.2017.05.010

[12]   Y. Bow, T. Dewi, HHO Gas Generation in Hydrogen Generator using Electrolysis, *IOP Conference Series: Earth and Environmental Science* **258** (2019) 012007. https://doi.org/10.1088/1755-1315/258/1/012007

[13]   K. Praveen, M. Sethumadhavan, On the extension of XOR step construction for optimal contrast grey level visual cryptography, *2017 International Conference on Advances in Computing, Communications and Informatics, ICACCI,* (2017) 219–222.

https://doi.org/10.1109/ICACCI.2017.8125843

[14]   M. H. Sellami, K. Loudiyi, Electrolytes behavior during hydrogen production by solar energy, *Renewable and Sustainable Energy Reviews* **70** (2017) 1331–1335. https://doi.org/10.1016/j.rser.2016.12.034

[15]   M. M. El-Kassaby, Y. A. Eldrainy, M. E. Khidr, K. I. Khidr, Effect of hydroxy (HHO) gas addition on gasoline engine performance and emissions, *Alexandria Engineering Journal* **55** (2016) 243–251. https://doi.org/10.1016/j.aej.2015.10.016

[16]   N. Alam, K. M. Pandey, Experimental Study of Hydroxy Gas (HHO) Production with Variation in Current, Voltage and Electrolyte Concentration, *IOP Conference Series: Materials Science and Engineering* **225** (2017) 012197. https://doi.org/10.1088/1757-899X/225/1/012197

[17]   R. Purwondho, A. Sudrajat, Handoko, Research on the effect of SS316L electrode plate treatment on HHO gas production performance, *IOP Conference Series: Earth and Environmental Science* **794** (2021) 012021. https://doi.org/10.1088/1755-1315/794/1/012021

[18]   I. Hamidah, A. Solehudin, A. Setiawan, A. Hamdani, M. A. S. Hidayat, F. Adityawarman, F. Khoirunnisa, A. B. D. Nandiyanto, Corrosion study of AISI 304 on KOH, NaOH, and NaCl solution as an electrode on electrolysis process, *Journal of Engineering Science and Technology* **13** (2018) 1345–1351.

[19]   B. Subramanian, S. Ismail, Production and use of HHO gas in IC engines, *International Journal of Hydrogen Energy* **43** (2018) 7140–7154. https://doi.org/10.1016/j.ijhydene.2018.02.120.

[20]   I. Hamidah, A. Solehudin, A. Setiawan, Effect of variation of kalium hydroxide solution concentration and temperature to the corrosion resistance of AISI 304, AISI 316, and copper alloys in water electrolysis apparatus, *ARPN Journal of Engineering and Applied Sciences* **11** (2016) 972–977.

[21]   J. M. Olivares-Ramírez, M. L. Campos-Cornelio, J. Uribe Godínez, E. Borja-Arco, R. H. Castellanos, Studies on the hydrogen evolution reaction on different stainless steels, *International Journal of Hydrogen Energy* **32** (2007) 3170–3173. https://doi.org/10.1016/j.ijhydene.2006.03.017

[22]   H. A. Abdulaah, A. M. Al-Ghaban, R. A. Anaee, A. A. Khadom, M. M. Kadhim, Cerium-tricalcium phosphate coating for 316L stainless steel in simulated human fluid: Experimental, biological, theoretical, and electrochemical investigations, *Journal of Electrochemical Science and Engineering* **13** (2023) 115-126. https://doi.org/10.5599/jese.1257

[23]   A. C. Schoeler, T. D. Kaun, I. Bloom, M. Lanagan, M. Krumpelt, Corrosion Behavior and Interfacial Resistivity of Bipolar Plate Materials under Molten Carbonate Fuel Cell Cathode Conditions, *Journal of The Electrochemical Society* **147** (2000) 916. https://doi.org/10.1149/1.1393292

[24]   M. Singh, H. Vasudev, M. Singh, Surface protection of SS-316L with boron nitride based thin films using radio frequency magnetron sputtering technique, *Journal of Electrochemical Science and Engineering* **12** (2022) 851–863. https://doi.org/10.5599/jese.1247

[25]   A. L. Yuvaraj, D. Santhanaraj, A systematic study on electrolytic production of hydrogen gas by using graphite as electrode, *Materials Research* **17** (2014) 83–87. https://doi.org/10.1590/S1516-14392013005000153

[26]   B. Amuzu-Sefordzi, J. Y. Huang, Effects of Increasing Alkali Catalysts Concentration on Hydrogen Gas Yield during the Supercritical Water Gasification of Food Waste, *Advanced Materials Research* **1073**–**1076** (2014) 905–910. https://doi.org/10.4028/www.scientific.net/amr.1073-1076.905

[27] P. Katsoufis, E. Doukas, C. Politis, G. Avgouropoulos, P. Lianos, Enhanced rate of hydrogen production by corrosion of commercial aluminum, *International Journal of Hydrogen Energy* **45** (2020) 10729–10734. https://doi.org/10.1016/j.ijhydene.2020.01.215

[28] X. L. Zhang, Z. H. Jiang, Z. P. Yao, Y. Song, Z. D. Wu, Effects of scan rate on the potentiodynamic polarization curve obtained to determine the Tafel slopes and corrosion current density, *Corrosion Science* **51** (2009) 581–587. https://doi.org/10.1016/j.corsci.2008.12.005

[29] Q. Liu, Q. Sun, S. Wang, K. Chen, Effect of scan rate on polarization curves of a high strength Al alloy in 3.5 wt% NaCl solution, *International Journal of Electrochemical Science* **16** (2021) 21113. https://doi.org/10.20964/2021.11.05

[30] Z. Ahmad, Principles of Corrosion Engineering and Corrosion Control, 1st ed., Butterworth-Heinemann, Oxford, United Kingdom, 2006. https://doi.org/10.1016/b978-0-7506-5924-6.x5000-4

[31] M. Talha, C. K. Behera, O. P. Sinha, Potentiodynamic polarization study of Type 316L and 316LVM stainless steels for surgical implants in simulated body fluids, *Journal of Chemical and Pharmaceutical Research* **4** (2012) 203–208.

[32] I. Gurappa, Characterization of different materials for corrosion resistance under simulated body fluid conditions, *Materials Characterization* **49** (2002) 73–79. https://doi.org/10.1016/S1044-5803(02)00320-0

[33] J. Wojciechowski, Ł. Kolanowski, A. Bund, G. Lota, The influence of current collector corrosion on the performance of electrochemical capacitors, *Journal of Power Sources* **368** (2017) 18–29. https://doi.org/10.1016/j.jpowsour.2017.09.069

[34] F. E. T. Heakal, O. S. Shehata, N. S. Tantawy, Integrity of metallic medical implants in physio-logical solutions, *International Journal of Electrochemical Science* **9** (2014) 1986–2004.

[35] W. M. F. W. Mohamad, M. Z. Selamat, B. Bundjali, M. Musa, Effect of cold rolling process on the microstructure and corrosion behaviors of 316L stainless steel in simulated body fluids, *Applied Mechanics and Materials* **548–549** (2014) 310–315. https://doi.org/10.4028/www.scientific.net/AMM.548-549.310

[36] F. B. Susetyo, B. Soegijono, Yusmaniar, M. C. Fajrah, M. Cahya, Deposition of nickel films on polycrystalline copper alloy with various current densities from watts solution Deposition of Nickel Films on Polycrystalline Copper Alloy with Various Current Densities from Watts Solution, *AIP Conference Proceedings* **2331** (2021) 030017. https://doi.org/10.1063/5.0041640

[37] R. Davalos, M. Jan, V.D.W. Benjamin, K. Dirk, Corrosion Behaviour of Type 316L Stainless Steel in Hot Caustic Aqueous Environments, *Metals and Materials International* **26** (2019) 630–640. https://doi.org/10.1007/s12540-019-00403-2

[38] F. Budhi Susetyo, A. Faridh, B. Soegijono, Stirring Effect on Surface Morphology, Structure, and Electrochemical Behavior of Electrodeposited Nickel Film on Copper Substrates, *IOP Conference Series: Materials Science and Engineering* **694** (2019) 012040. https://doi.org/10.1088/1757-899X/694/1/012040

[39] Z. Feng, X. Cheng, C. Dong, L. Xu, X. Li, Passivity of 316L stainless steel in borate buffer solution studied by Mott-Schottky analysis, atomic absorption spectrometry and X-ray photoelectron spectroscopy, *Corrosion Science* **52** (2010) 3646–3653. https://doi.org/10.1016/j.corsci.2010.07.013

[40] F. Nasirpouri, M. R. Sanaeian, A. S. Samardak, E. V. Sukovatitsina, A. V. Ognev, L. A. Chebotkevich, M. G. Hosseini, M. Abdolmaleki, An investigation on the effect of surface morphology and crystalline texture on corrosion behavior, structural and magnetic properties of electrodeposited nanocrystalline nickel films, *Applied Surface Science* **292** (2014) 795–805. https://doi.org/10.1016/j.apsusc.2013.12.053

[41]   B. Krawczyk, P. Cook, J. Hobbs, D. L. Engelberg, Corrosion behavior of cold rolled type 316L stainless steel in HCl-containing environments, *Corrosion* **73** (2017) 1346–1358. https://doi.org/10.5006/2415

[42]   X. Fang, H. Zhou, Y. Xue, Corrosion properties of stainless steel 316L/Ni–Cu–P coatings in warm acidic solution, *Transactions of Nonferrous Metals Society of China* **25** (2015) 2594–2600. https://doi.org/10.1016/S1003-6326(15)63880-8

[43]   A. Hossain, F. Gulshan, A. S. W. Kurny, Electrochemical corrosion behavior of Ni-containing hypoeutectic Al-Si alloy, *Journal of Electrochemical Science and Engineering* **5** (2015) 173–179. https://doi.org/10.5599/jese.174

[44]   A. Fattah-Alhosseini, A. Saatchi, M. A. Golozar, K. Raeissi, The passivity of AISI 316L stainless steel in 0.05 M H_2SO_4, *Journal of Applied Electrochemistry* **40** (2010) 457–461. https://doi.org/10.1007/s10800-009-0016-y

[45]   J. Huang, X. Wu, E. H. Han, Influence of pH on electrochemical properties of passive films formed on Alloy 690 in high temperature aqueous environments, *Corrosion Science* **51** (2009) 2976–2982. https://doi.org/10.1016/j.corsci.2009.08.002

[46]   T. Dan, T. Shoji, Z. Lu, K. Sakaguchi, J. Wang, E. H. Han, W. Ke, Effects of hydrogen on the anodic behavior of Alloy 690 at 60 °C, *Corrosion Science* **52** (2010) 1228–1236. https://doi.org/10.1016/j.corsci.2009.11.039.

[47]   A. Fattah-Alhosseini, S. Vafaeian, Comparison of electrochemical behavior between coarse-grained and fine-grained AISI 430 ferritic stainless steel by Mott-Schottky analysis and EIS measurements, *Journal of Alloys and Compounds* **639** (2015) 301–307. https://doi.org/10.1016/j.jallcom.2015.03.142

[48]   N. B. Hakiki, S. Boudin, B. Rondot, M. Da Cunha Belo, The electronic structure of passive films formed on stainless steels, *Corrosion Science* **37** (1995) 1809–1822. https://doi.org/10.1016/0010-938X(95)00084-W

[49]   C. Sunseri, S. Piazza, F. Di Quarto, Photocurrent Spectroscopic Investigations of Passive Films on Chromium, *Journal of The Electrochemical Society* **137** (1990) 2411–2417. https://doi.org/10.1149/1.2086952

[50]   H. R. Ghorbani, F. P. Mehr, H. Pazoki, B. M. Rahmani, Synthesis of ZnO nanoparticles by precipitation method, *Oriental Journal of Chemistry* **31** (2015) 1219–1221. https://doi.org/10.13005/ojc/310281

[51]   S. Jain, A. Jain, P. Kachhawah, V. Devra, Synthesis and size control of copper nanoparticles and their catalytic application, *Transactions of Nonferrous Metals Society of China (English Edition)* **25** (2015) 3995–4000. https://doi.org/10.1016/S1003-6326(15)64048-1

[52]   M. El-Kemary, N. Nagy, I. El-Mehasseb, Nickel oxide nanoparticles: Synthesis and spectral studies of interactions with glucose, *Materials Science in Semiconductor Processing* **16** (2013) 1747–1752. https://doi.org/10.1016/j.mssp.2013.05.018

[53]   M. Lu, Y. Cui, S. Zhao, A. Fakhri, Cr_2O_3/cellulose hybrid nanocomposites with unique properties: Facile synthesis, photocatalytic, bactericidal and antioxidant application, *Journal of Photochemistry and Photobiology B: Biology* **205** (2020) 111842. https://doi.org/10.1016/j.jphotobiol.2020.111842

[54]   Z. S. Ma, H. L. Ding, Z. Liu, Z. L. Cheng, Preparation and tribological properties of hydrothermally exfoliated ultrathin hexagonal boron nitride nanosheets (BNNSs) in mixed NaOH/KOH solution, *Journal of Alloys and Compounds* **784** (2019) 807–815. https://doi.org/10.1016/j.jallcom.2019.01.108

[55]   S. Nasrazadani, J. Diaz, J. Stevens, R. Theimer, Effects of DBU, morpholine, and DMA on corrosion of low carbon steel exposed to steam, *Corrosion Science* **49** (2007) 3024–3039. https://doi.org/10.1016/j.corsci.2007.01.012

[56]   H. Du, Y. Cheng, L. Hou, Y. Li, Y. Wei, Evolution of intergranular corrosion resistance for HR3C heat-resistant austenitic stainless steel at elevated temperature, *Corrosion Engineering Science and Technology* **52** (2017) 343–348. https://doi.org/10.1080/1478422X.2017.1291119

[57]   Y. R. Galindo-Luna, A. Torres-Islas, R. J. Romero, M. Montiel-González, S. Serna, Corrosion behavior of AISI 316L stainless steel in a NaOH-H_2O mixture, *International Journal of Electrochemical Science* **13** (2018) 631–641. https://doi.org/10.20964/2018.01.64

[58]   Y. Cai, X. Luo, M. Maclean, Y. Qin, M. Duxbury, F. Ding, A single-step fabrication approach for development of antimicrobial surfaces, *Journal of Materials Processing Technology* **271** (2019) 249–260. https://doi.org/10.1016/j.jmatprotec.2019.04.012